Radiative muon capture on Al, Si, Ca, Mo, Sn, and Pb

D. S. Armstrong,[1,*] A. Serna-Angel,[1,†] S. Ahmad,[2,‡]
G. Azuelos,[3,4] W. Bertl,[5] M. Blecher,[1] C. Q. Chen,[3]
P. Depommier,[4] T. von Egidy,[3,§] T. P. Gorringe,[6]
M. D. Hasinoff,[2] R. S. Henderson,[3,7] A. J. Larabee,[2,**]
J. A. Macdonald,[3] S. C. McDonald,[7] J-M. Poutissou,[3]
R. Poutissou,[3] B. C. Robertson,[8] D. G. Sample,[2]
G. N. Taylor,[7] D. H. Wright,[3] and N. S. Zhang[3]

[1] *Virginia Polytechnic Institute and State University, Blacksburg, Virginia 24061*
[2] *University of British Columbia, Vancouver, British Columbia, Canada V6T 1Z5*
[3] *TRIUMF, Vancouver, British Columbia, Canada V6T 2A3*
[4] *Université de Montréal, Montréal, Québec, Canada H3C 3J7*
[5] *Paul Scherrer Institute, CH-5234, Villigen, Switzerland*
[6] *University of Kentucky, Lexington, Kentucky 40506*
[7] *University of Melbourne, Parkville, Victoria, Australia 3001*
[8] *Queen's University, Kingston, Ontario, Canada K7L 3N6*

(Received 5 May 1992)

The branching ratio for radiative muon capture (RMC), relative to the nonradiative process, is sensitive to g_p, the induced pseudoscalar coupling constant of the weak hadronic current. The photon energy spectra from RMC on ^{27}Al, ^{28}Si, ^{40}Ca, ^{nat}Mo, ^{nat}Sn, and ^{nat}Pb have been measured using a high-acceptance pair spectrometer. The measured partial branching ratios, R_γ, for photons of $E_\gamma >$ 57 MeV are 1.43 ± 0.13, 1.93 ± 0.18, 2.09 ± 0.19, 1.11 ± 0.11, 0.98 ± 0.09, and 0.60 ± 0.07 respectively, in units of 10^{-5}. The results confirm the previously observed suppression of R_γ with increasing Z for $Z > 20$. For ^{40}Ca the present result is in good agreement with previous measurements. For the heavier nuclei, the results are compared with two recent calculations performed in the Fermi-gas model. In one case the data indicate a complete quenching of g_p, but the more recent calculation does not reproduce the data for any value of g_p.

PACS number(s): 23.40.Bw, 13.10+q

I. INTRODUCTION

For semileptonic weak processes, the V-A structure of the weak interaction is modified by the so-called "induced" weak currents [1] which arise due to the presence of the strong interaction. The least well measured of these is the pseudoscalar weak current. The process of radiative muon capture (RMC) is of interest primarily because of its sensitivity to the magnitude of the induced pseudoscalar coupling constant, g_p. The prediction that $g_p/g_a = 6.8$ for the proton[1] [2], where g_a is the axial coupling constant, arises from the partially conserved axial-vector current hypothesis (PCAC) and the Goldberger-Treiman relation [3]. A precision measurement of g_p tests these basic ideas. The elementary process $\mu^- p \rightarrow \nu_\mu n \gamma$ is presently being measured at TRIUMF, but only very preliminary results are available [4, 5]. However, there have been measurements of the branching ratios for RMC in several nuclei with $Z \geq 6$. The value of g_p extracted from nuclear RMC measurements could differ from the nucleonic value, and such deviations could signal a renormalization of the pseudoscalar coupling, similar to the apparent quenching of g_a in nuclei [6–9]. However, the extraction of g_p from nuclear RMC measurements requires that the nuclear response function be correctly treated. If one measures the experimental RMC branching ratio relative to the ordinary (nonradiative) muon capture process (OMC), and compares it with the results of a calculation in which both RMC and OMC have been calculated in a consistent way, then the dependence on the detailed nuclear structure will be reduced, but not totally eliminated.

Experimental work on RMC has a thirty year history [10], but only recently have reliable data become available, largely through the use of photon converters, in conjunction with either NaI detectors [11–13] or pair spectrometers [14, 15]. Despite this, data on RMC branching ratios exist for only a handful of nuclei scat-

*Present address: University of California, Lawrence Berkeley Lab., Berkeley, CA 94720.
†Present address: Universidad Tecnologica de Pereira, Pereira, Colombia.
‡Present address: Rice University, Houston, TX 77251.
§Also at Technische Universität München, D-8046, Garching, Germany.
**Present address: Buena Vista College, Storm Lake, IA 50588.

[1] This is evaluated at the momentum transfer appropriate for ordinary muon capture.

tered throughout the periodic table. The nucleus ^{40}Ca is a benchmark where there is good agreement on the RMC/OMC branching ratio from several different experiments [11–15]. The five most recent measurements all yield values consistent with a partial branching ratio of 2.1×10^{-5} for photons with energies greater than 57 MeV. Comparing this with theory yields a value for g_p consistent with, or slightly lower than, the PCAC prediction of $6.8 g_a$, depending on the calculation adopted [15]. Data are also available for two light nuclei, ^{16}O [12, 15–17] and ^{12}C [12, 15]. Here there are disagreements among the different measurements of the branching ratios and also large differences among theoretical calculations which lead to very different values of g_p being obtained from the same branching ratio. For example, from the most precise measurement for ^{16}O one obtains the values $g_p/g_a = 7.3 \pm 0.9$, 9.1 ± 0.9, and $13.6^{+1.6}_{-1.9}$ when compared with three different recent calculations of the nuclear response [15, 16].

The only measured RMC branching ratios for nuclei with $Z > 20$ are from Döbeli *et al.* [12] who measured RMC on ^{nat}Fe, ^{165}Ho, and ^{209}Bi, as well as ^{40}Ca, ^{27}Al, ^{16}O, and ^{12}C. These results indicate an intriguing systematic reduction in the RMC branching ratio with increasing atomic number. When compared with a Fermi-gas model calculation of the nuclear response [18] these data indicate a quenching of g_p to zero for $Z \sim 80$.

To investigate this trend, we have measured the branching ratio for inclusive RMC on ^{27}Al, ^{28}Si, ^{40}Ca, ^{nat}Mo, ^{nat}Sn, and ^{nat}Pb, using a pair spectrometer to detect the high-energy photons from RMC. The spectrometer consisted of a large-volume drift chamber surrounding a Pb photon converter. The usefulness of a large-acceptance pair spectrometer for measurements of RMC has been demonstrated in earlier work [15, 16].

II. EXPERIMENT

A. Muon and pion beams

The experiment was mounted at the M9A stopped-π/μ channel at TRIUMF. The primary beam consisted of 500 MeV protons with a typical current between 100 and 140 μA, a microstructure of 5-ns-long pulses every 43.3 ns, and a macroscopic duty factor of 100%. A 65 MeV/c cloud μ^- beam was used, with a raw beam composition of $\pi/\mu \sim 1$ and $e/\mu \sim 10$ at the detector. A radio frequency particle separator [19] was used to suppress both the electron and pion content in the muon beam. The separated beam composition was measured to be $\pi/\mu \sim 10^{-3}$ and $e/\mu \sim 5 \times 10^{-2}$. The negative muon flux incident on the beam counters was 6.0×10^5 s^{-1} with $\delta P/P$ =10% and with a spot size of 5×5 cm^2; the typical μ^- stopping rate in the targets was 5.0×10^5 s^{-1}. A 65 MeV/c μ^+ beam was also used for background studies. An 81 MeV/c π^- beam was used for detector calibration purposes, with a typical beam composition after the separator of 96.3% π^-, 2.9% e^-, 0.8% μ^-.

B. Targets

The targets used for the RMC data-taking were natural Al, Si, Ca, Mo, Sn, and Pb. The dimensions of the targets are given in Table I. The higher-Z targets were segmented into foils, separated along the beam direction so as to minimize photon conversion in the target while still stopping the beam. The Si target was made of granulated Si encased in a thin-walled polystyrene container. The Al target was made from an alloy (6063 Al) which contains a total fraction of $\sim$ 1.8% of various alloying elements, primarily Mg and Si; no correction has been made in the results for the effect of these impurities.

For calibration data-taking a 3-liter liquid hydrogen target was used [20]. This target was cylindrical, 16 cm in diameter and 15 cm in length. The target walls were 254-μm-thick gold, and the target was surrounded by two silver heat shields each 127 μm thick, and a 254-μm-thick silver vacuum vessel. A 15.3-cm-diameter, 1.9-cm-thick disk of graphite was also used as a ^{12}C target for calibration purposes.

C. Drift chamber

The e^+e^- pairs produced by the conversion of RMC photons in a 1.08 mm Pb sheet were momentum-analyzed using a large-volume cylindrical drift chamber in a uniform magnetic field of 0.275 T. The chamber consists of four super-layers of drift cells, each cell possessing six sense wires. The wires of layers 1, 2, and 4 are axial and those of layer 3 are inclined at a stereo pitch angle of 7° (relative to axial) to provide a z coordinate for each track. The four layers have 56, 64, 72, and 80 cells, respectively, for a total of 1632 instrumented sense wires. The sense wires are staggered ± 254 μm about the cell

TABLE I. Dimensions of the targets used. All targets were mounted perpendicular to the beam axis.

Target	Shape	Dimensions	No. of foils	Spacing of foils
Pb	rectangular	15.0 cm × 13.5 cm × 0.020 cm	10	0.94 cm
Sn	square	12.5 cm × 12.5 cm × 0.033 cm	11	1.0 cm
Mo	square	12.5 cm × 12.5 cm × 0.025 cm	7	1.1 cm
Ca	square	10.2 cm × 10.2 cm × 1.96 cm	1	
Al	disk	15.0 cm diam × 1.92 cm thick	1	
Si	disk	8.4 cm diam × 2.00 cm thick	1	

midplane to provide local resolution of the left-right ambiguity. The sense wire discriminators are read out by LeCroy 1879 FASTBUS pipeline TDC's which provide multihit time information in 2 ns bins for each wire hit. The gas mixture used is 49.9% argon, 49.9% ethane, and 0.2% ethanol, which provides a drift velocity of about 52 μm/ns at the operating voltage. Full efficiency is obtained at operating voltages of 5.0, 5.1, 5.2, and 5.3 kV on layers 1, 2, 3, and 4 respectively. The axial magnetic field was provided by a large solenoidal conventional magnet. The field uniformity over the active volume of the drift chamber is $\pm 0.5\%$. More information on the design and performance of the drift chamber can be found elsewhere [21, 20, 22].

D. Inner wire chamber

Located inside the inner radius of the drift chamber is the inner wire chamber (IWC), a dual-coordinate cylindrical proportional chamber of the type described by Bird *et al.* [23]. The z coordinate from the IWC is used along with the z coordinate determined from the stereo layer of the drift chamber to determine the longitudinal component of the momentum of each track. It has 768 anode wires strung parallel to the beam direction, and two planes of cathodes. Each plane consists of 384 aluminized Mylar strips, inclined at an angle of $+45°$ and $-45°$ degrees relative to the anode wires for the inner and outer cathode planes, respectively. The IWC provides an (x, y, z) point for each hit. The (x, y) coordinates are obtained from the anode wire location with 600 μm (σ) resolution, and the z coordinate from the intersection of the anode and the hits on the two cathode planes, with 1.2 mm (σ) resolution. Details on the IWC are available elsewhere [20, 23].

E. Beam and trigger counters

Four scintillation counters, each 1.6 mm in thickness, were located approximately 17 cm upstream of the target center. These were used to count the incident μ^- beam, and in offline analysis to reject π^--induced events. Each of these beam counters was read out via two separate light guides and photomultiplier tubes. A cylindrical disk scintillation counter (V) 23.3 cm in diameter and 6.4 mm thick, read out via an air light-guide and a single photomultiplier, was located behind the solid targets to complete the definition of a muon stop.

Four concentric layers of scintillation counters surrounded the target region. The first two layers were circular tubes of 3.2-mm-thick scintillators (A_{1-4} and A'_{1-4}), each consisting of four arc segments. The joints between the segments were offset by 45° between the two layers to cover the gaps. These counters were used to veto charged particles (primarily muon-decay electrons) coming from the target.

The next two layers (B_{1-12} and C_{1-12}) consisted of polygonal tubes, each made up of 12 flat panels, which were 3.2 mm thick. Sandwiched between these two layers was the 1.08-mm-thick Pb photon converter. The B layer served as an additional charged-particle veto and the C layer was used to identify photon conversions. Outside the drift chamber was a polygonal tube of 16 scintillators D_{1-16}, each 6.4 mm thick. Each scintillation counter was optically isolated from its neighbors and read out via a light guide and photomultiplier. All the phototubes were located outside the spectrometer magnet on the upstream side, except those for the A and A' counters which were on the downstream side.

Covering the magnet were counters to veto cosmic-ray-induced events. The top and all four sides of the magnet were covered by a double layer of planar drift chambers and a single layer of scintillators.

F. Trigger and data acquisition

The complete photon trigger was performed at several levels in hardware and software. The first level was the hardware coincidence $\overline{\Sigma(\mathrm{A}+\mathrm{A}')} \cdot \overline{\Sigma \mathrm{B}} \cdot \Sigma \mathrm{C} \cdot \geq 2\mathrm{D}$, i.e., no hits in the veto scintillation counters inside the diameter of the Pb converter, at least one hit in the C scintillators, indicating a photon conversion, and at least two D scintillators hit, indicating an e^+e^- pair. This trigger therefore required that both tracks from the converted pair pass through the entire drift chamber. The second-level hardware trigger required that at least two of the struck D counters have the correct spatial orientation, relative to the C counter(s) hit, to be characteristic of a valid converted photon.

When the two levels of hardware trigger were satisfied, the FASTBUS TDC's were provided with a common stop signal and began their conversion, and the front-end microprocessor began the data readout. This FASTBUS microprocessor is the SLAC scanner processor (SSP) [24] which handled the readout of all the FASTBUS and CAMAC modules. In addition it provided two more levels of trigger requirements in software. The first of these put restrictions on the pattern of cells hit in the drift chamber, determined from custom-built trigger cards [25] connected to the FASTBUS TDC's. The last level of trigger required that the IWC have a sufficient number of data words to be a valid event. If either of these conditions was not present, then the TDC conversion was interrupted, all modules were cleared, and the system reenabled. Otherwise the event was read out and stored in a buffer. Data buffers were read by a μVAX II, stored in shared memory for online analysis and written to magnetic tape for off-line analysis.

In parallel with the photon trigger, special triggers were enabled to provide samples of charged particles originating in the target and samples of any event in which at least two of the beam counters fired; these data were used to monitor the efficiencies of the trigger counters and the beam composition respectively. More details on the trigger and data acquisition can be found elsewhere [20].

III. DATA ANALYSIS

A. Event selection

Various selection criteria ("cuts") were applied to the data to reject background events and poorly fitted tracks.

The cuts were based on the characteristics of the tracks in the drift chamber, as well as on information from the trigger counters, beam counters, and cosmic-ray counters. The efficiencies of the cuts were determined using both the pion calibration data and simulated data from the Monte Carlo program. The same cuts were applied to the RMC data, the pion calibration data and Monte Carlo data, with the exception of the "prompt" veto (see below), which was inappropriate for the pion calibration data.

The cuts applied to the data are summarized as follows:

(1) Track fitting: minimum number of points per track; maximum χ^2 for the fitted track; maximum fractional momentum in the longitudinal (z) direction; maximum difference between the location of the track at the IWC determined from the drift chamber and that determined from the IWC hit; minimum number of points in the track in the fourth (outer) superlayer of the drift chamber.

(2) Trigger: the hardware trigger requirements are reimposed on the data in software; each track in the pair must project to, and fire the appropriate D scintillator; there must have been an incident μ in the previous 10 μs; there must not have been another charged particle in the same region of the drift chamber within $\pm$100 ns of the photon.

(3) Cosmic ray veto: rejection based on various combinations of cosmic-ray veto counters and trigger counters in coincidence with the event.

(4) Geometry: maximum opening angle of the pair; maximum difference in both azimuthal angle (ϕ) and axial position (z) between the two tracks of the pair at the converter; maximum distance in z between the photon conversion point and the target center; maximum distance of closest approach of the photon to the target center, in both z and the transverse plane.

(5) Prompt (pion) veto: rejection of events in prompt coincidence with hits in the beam counters; this cut is discussed in more detail below.

A typical event passing all cuts is shown in Fig. 1.

B. Detector response

The photon response function was determined using the GEANT Monte Carlo simulation program [26]. Monoenergetic photons were generated at 10 MeV intervals between 50 and 140 MeV; typically 2×10^5 photons were generated at each energy. The simulated events were analyzed as actual data, and the reconstructed photon energy spectra were fitted to an analytic parametrization, which is described in the appendix.

Rather than relying solely on GEANT to predict the absolute normalization of the detector acceptance, the normalization was determined using (π^-, γ) calibration data. The Monte Carlo simulation was tested by comparing the experimental spectrum from radiative pion capture on ^{12}C with the Monte Carlo prediction using the high-resolution spectrum of Perroud *et al.* [27] for the input (see Fig. 2). The branching ratio for $^{12}C(\pi^-, \gamma)$ used in the Monte Carlo simulation was $(1.83 \pm 0.06)\%$ [27, 28]. The Monte Carlo acceptance had to be reduced by 7.2% to match the data. This factor is in reasonable agreement with estimates of various inefficiencies in the detector that are not incorporated into the GEANT simulation. Similar good agreement in spectral shape is found between the data and Monte Carlo predictions for the reactions [29]

$$\pi^- p \rightarrow \pi^0 n, \tag{1}$$

$$\pi^- p \rightarrow \gamma n, \tag{2}$$

at rest, obtained experimentally by stopping a π^- beam in the hydrogen target. The radiative capture gamma ray [Eq. (2)] has an energy of 129.4 MeV, and the π^0 decays primarily into two photons (98.8% branch) yielding a uniform photon energy spectrum between 54.9 MeV and 83.0 MeV. The comparison is shown in Fig. 3. Here the data have been normalized in an arbitrary way to match the Monte Carlo prediction. This is due to difficulties in determining the actual number of π^- stops in the hydrogen, because of the unknown fraction that stopped in the walls of the hydrogen target. An energy calibration error of $\pm$500 keV was estimated from the comparisons between GEANT-simulated data and the data for both the $\pi^- p$ and $^{12}C(\pi^-,\gamma)$ reactions.

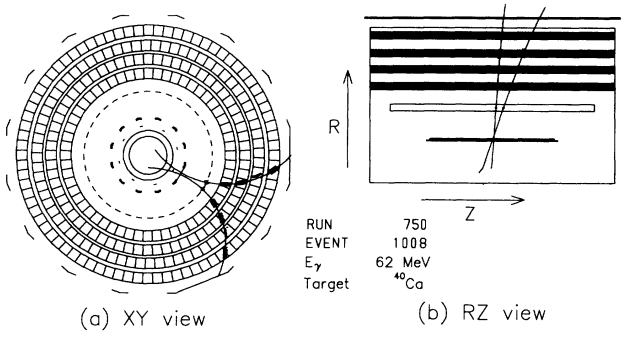

FIG. 1. Graphical representation of a typical photon conversion event from radiative muon capture.

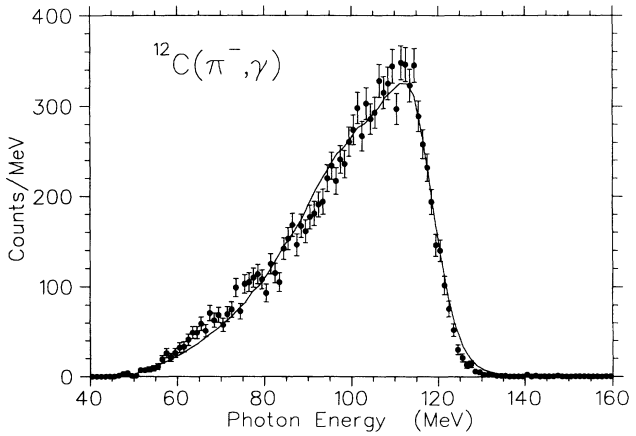

FIG. 2. Photon energy spectrum from the reaction $^{12}C(\pi^-, \gamma)$ compared with the Monte Carlo simulation. The data are given by the smooth line and the solid circles are the Monte Carlo results.

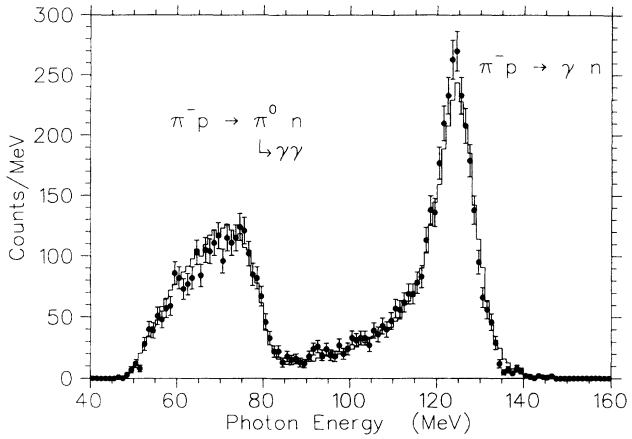

FIG. 3. Photon energy spectrum from the reactions $\pi^- p \rightarrow \gamma n$ and $\pi^- p \rightarrow \pi^0 n$, $\pi^0 \rightarrow 2\gamma$ obtained from π^- stopping in liquid hydrogen (histogram), compared with the Monte Carlo simulation (solid circles).

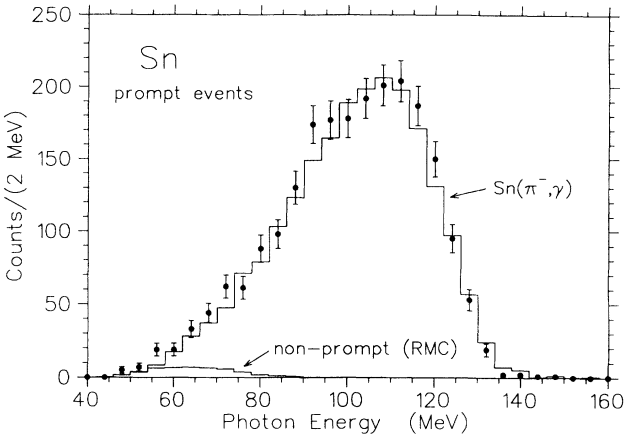

FIG. 4. Photon energy spectrum of "prompt" events from the Sn target (solid circles) compared with the fitted contributions from the $\mathrm{Sn}(\pi^-, \gamma)$ process and the nonprompt energy spectrum (primarily RMC).

C. Backgrounds

1. *Pion capture*

Radiative pion capture is a potentially serious background, as its branching ratio is typically $\sim 2 \times 10^{-2}$ [28], several orders of magnitude larger than the signal from RMC ($\sim 10^{-5}$ per captured muon). The rf separator reduced the π/μ ratio in the beam to approximately 10^{-3}. Most of the remaining pions stopped in the beam counters rather than reaching the target. Finally, photon events in prompt coincidence with an incident beam particle were rejected in the off-line software. Due to the short μ^- lifetime in the high-Z targets (75 ns for Pb), care had to be taken with the cuts used to eliminate prompt events, so as to minimize the number of good RMC events rejected. A set of conditions based on the ADC's and TDC's of the beam scintillators were adopted, which utilized the difference in dE/dx and time-of-flight between incident muons and pions. If the event was preceded within the previous 20 ns by an incident particle having the time-of-flight characteristic of a muon, the event was rejected only if two or more of the four beam counter ADC's registered signals 1.5σ larger than those characteristic of the majority of muons. This allowed even an RMC event occurring in prompt coincidence with the μ^- arrival to be accepted. Otherwise, the event was rejected if any one ADC value was over this threshold. Finally, if any of the beam counter signals were more than 4σ above the muon pulse height, indicating a π^- stopping in one of the counters, the event was rejected regardless of the time-of-flight of the incident particle.

The efficiency for π^- rejection was determined by examining the photon events above the $\sim$ 100 MeV end point for RMC, before and after the prompt cuts, after all other cuts were applied. Attributing these events to the (π^-, γ) process indicates a rejection efficiency of 99.3%. For all targets, less than 0.7% of the photon energy spectrum consisted of (π^-, γ) events that survived the prompt cut.

The fact that the energy spectra from RMC and (π^-, γ) have different shapes was also used to determine the number of otherwise acceptable RMC events that were lost due to the prompt cuts. The (π^-, γ) spectra were determined for each target in separate runs with the beam tuned to provide stopping π^-'s. For each target, a χ^2-fit was made of the energy spectrum of events rejected by the prompt cuts (passing all other cuts) to a weighted sum of the (π^-, γ) spectrum and the nonprompt RMC spectrum. An example of such a fit is shown in Fig. 4. The weighting factor for the nonprompt spectrum yields the fraction of RMC events in the prompt spectrum, i.e. those that were falsely rejected (see Table II). In all cases this was less than $\sim$ 2%.

2. *Cosmic rays*

A low rate of candidate photons was observed arising from electromagnetic showers induced by cosmic rays. The majority of these events were easily rejected using the information provided by the cosmic-ray veto scintillation counters and drift chambers surrounding the magnet, or by the geometrical cuts applied that required the photon to originate in the target. The rate of cosmic-ray photons that survived the cuts was determined to be 2.3 ± 0.4 events/day in the energy region of interest (57 to 100 MeV), based on 320 hours of background data collected between and after various data-taking runs. This is a small background (< 0.4%) for all targets; see Table II.

3. *Muon stops outside the target*

RMC from muons that stopped in the scintillators surrounding the target (A, V) rather than in the target is also a source of background. The fraction of the μ^- beam

TABLE II. Correction factors applied to the number of observed photons above 57 MeV ($N^{\gamma}_{>57}$). Each entry is a multiplicative factor to be applied to $N^{\gamma}_{>57}$. Prompt rejection refers to real RMC events rejected by the prompt cut. Random vetoing refers to events rejected by the A, A', B veto scintillators or the cosmic ray cut.

Target	Photon absorption	Random vetoing	Prompt rejection	(π^-, γ)	RMC from scintillators	Cosmic rays
Al	1.32±0.04	1.079±0.006	1.000±0.004	0.996±0.002	0.987±0.006	0.998±0.001
Si	1.15±0.03	1.070±0.005	1.021±0.005	0.998±0.001	0.966±0.015	0.998±0.001
Ca	1.26±0.04	1.058±0.005	1.019±0.005	0.997±0.001	0.992±0.004	0.999±0.001
Mo	1.18±0.03	1.086±0.009	1.006±0.004	0.996±0.002	0.979±0.010	0.998±0.001
Sn	1.19±0.03	1.085±0.006	1.014±0.007	0.998±0.002	0.975±0.013	0.998±0.001
Pb	1.26±0.04	1.053±0.008	1.016±0.011	0.993±0.003	0.966±0.017	0.996±0.001

that was scattered into these scintillators was monitored in hardware scalers and checked using the events from the beam-sample trigger. The contribution to the RMC spectrum for each target was then estimated using the RMC rate from carbon [15] (μ^- capture on the hydrogen in the scintillators is negligible) after correcting for the geometrical reduction in acceptance for photons originating in the scintillators, which was estimated using the GEANT Monte Carlo simulation. This background was 1–4% of the RMC signal, depending on the target; see Table II. Confirmation of the small size of this background was obtained by fitting the time distribution of the RMC events, relative to the muon arrival time, taking into account the effect of pileup of the incident muons [22]. Good agreement was found with the literature values for the μ^- lifetimes in each target [30], with no need to include a significant contribution having the lifetime of muons in carbon.

4. *Bremsstrahlung*

The region of the photon energy spectrum below 53 MeV is contaminated by unavoidable background due to muon-decay events. This arises from radiative muon decay ($\mu^- \rightarrow e^- \overline{\nu_e} \nu_\mu \gamma$) and from the bremsstrahlung of muon-decay electrons in the target and surroundings. For a free μ^- the photon spectrum from each of these processes has a kinematic end point of 53 MeV, thus RMC measurements typically utilize only that portion of the spectrum above 57 MeV (allowing for detector resolution). However, both distortions in the decay electron spectrum due to muon binding and any high-energy tail in the photon energy resolution of the detector could produce events above 57 MeV.

To search for any high-energy tail in the detector response, data were obtained with a μ^+ beam stopping in the target. This "turns off" the muon capture process but retains the muon-decay processes, and is therefore very useful for searching for backgrounds.[2] The photon energy spectrum obtained, after all cuts, is displayed in Fig. 5. There are no photons below about 43 MeV since the detector acceptance falls to zero there, due to the trigger requirement that the e^+e^- pair reaches the D (outer) scintillators. There are only two photon events above 57 MeV, quite consistent with the 2.0 ± 0.8 cosmic ray background events expected in 21 hours live time. Thus the high-energy tail on the detector resolution is negligible.

One cut that was essential to ensure such a small high-energy tail was the rejection of any event with a charged particle in the chamber within ±100 ns of the photon trigger. This cut was imposed by examining the multihit TDC spectra for the trigger scintillators for coincidences indicative of an early or late charged particle. This cut was required to reject false events where a low-energy photon, from bremsstrahlung, for example, converts with very asymmetric energy sharing between the e^+ and e^-, such that only one of the particles escapes the Pb converter and is tracked in the detector. In near coincidence, another muon decay produces a second track in the chamber. If the time of emission of this electron is close enough to the time of the first tracked particle, but not within the (±30 ns) hardware veto window, and if

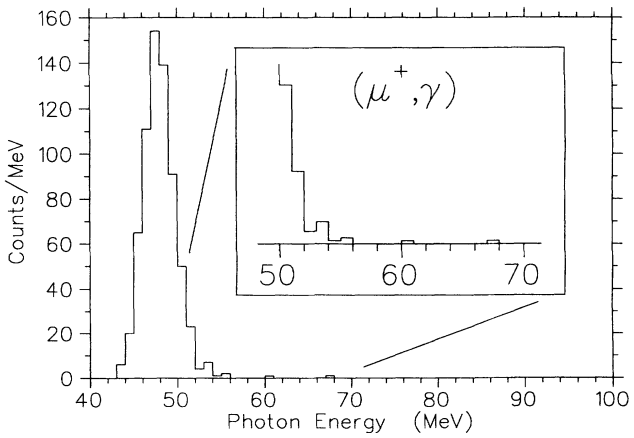

FIG. 5. Photon energy spectrum from μ^+'s stopping in liquid hydrogen. The two events above 57 MeV are consistent with the measured cosmic ray background.

[2]The effect of the additional process of e^+ annihilation-in-flight on the shape of the photon energy spectrum was determined by Monte Carlo simulation, and was found to be small.

the direction of the electron is close enough to that of the photon, then an acceptable vertex is reconstructed and the event appears as a "photon" of much higher energy than the photon that actually caused the trigger. This somewhat improbable chain of events would cause a significant high-energy tail in the detector response, unless the cut described above is imposed. The relatively large high-energy tail seen in our previous RMC measurements using a time projection chamber [15] was likely to be at least partly due to this pathology. A similar cut was not imposed in that experiment because of the lack of multihit TDC information from the trigger scintillators.

The high-energy tail (above 57 MeV) of the radiative μ-decay and bremsstrahlung spectrum due to muon binding effects was estimated using the decay electron spectra provided by Hänggi *et al.* [31] [Eq. (13) of Ref. [31], corrected according to Herzog and Alder [32]]. The bremsstrahlung spectra from decay electrons in each target was generated using GEANT, along with the radiative decay spectrum [33]. In each case the contribution to the photon energy spectrum above 57 MeV was found to be negligible ($< 0.1\%$) relative to the RMC signal. Indeed, for most targets even the region below 57 MeV was dominated by RMC rather than bremsstrahlung photons.

D. Branching ratio calculation

The observed photon energy spectrum $dN_\gamma(E)/dE$ from RMC is related to the physical photon energy spectrum per muon capture $d\Lambda(E_\gamma)/dE_\gamma$ by

$$\frac{dN_\gamma(E)}{dE} = N_\mu f_{\rm cap} \int dE_\gamma \, D(E_\gamma, E) \, \frac{d\Lambda(E_\gamma)}{dE_\gamma} \quad , \quad (3)$$

where N_μ is the (dead-time corrected) number of muon stops in the target, $f_{\rm cap}$ is the fraction of muons that undergo nuclear muon capture and $D(E_\gamma, E)$ is the detector response function (see appendix) defined as the probability that a photon with energy E_γ is detected and reconstructed at an energy E. This relation implicitly defines the observable $d\Lambda(E_\gamma)/dE_\gamma$ in terms of known or measured quantities. In principle, knowledge of $D(E_\gamma, E)$ would allow Eq. (3) to be inverted, and the physical photon spectrum extracted from the observed spectrum. In practice, with low statistics on the observed spectrum, this deconvolution process is not unique, and it produces unphysical fluctuations in the deconvoluted spectrum. Instead, the method used is to choose a theoretical photon energy spectrum $d\Lambda(E_\gamma)/dE_\gamma$, convolute it with the detector response function, and compare it with the measured spectrum.

The number of photon events above an observed energy of 57 MeV

$$N^\gamma_{>57} = \int_{57} dE \frac{dN_\gamma(E)}{dE} \quad (4)$$

can be considered as a function of the theoretical partial branching ratio for photons above 57 MeV

$$R_\gamma = \int_{57} dE_\gamma \frac{d\Lambda(E_\gamma)}{dE_\gamma} \quad , \quad (5)$$

which is given in units of photons/capture. Alternatively, $N^\gamma_{>57}$ can be considered as a function of g_p. Thus g_p or R_γ can be determined by comparing the number of photons predicted above 57 MeV for various values of g_p (or R_γ) with the experimental value of $N^\gamma_{>57}$. For a given calculation of the nuclear response, the full theoretical photon energy spectrum was convoluted with the detector acceptance and response function, integrated above 57 MeV, and then multiplied by N_μ to give the predicted number of counts above 57 MeV. To this extent, not only the rate but the shape of the spectrum is used in the determination of g_p from the data. Simple polynomial fits were made to the predicted $N^\gamma_{>57}$ as a function of R_γ and as a function of g_p/g_a; these were then compared with the measured $N^\gamma_{>57}$ to determine g_p/g_a and R_γ.

To extract the RMC branching ratio from the data, $N^\gamma_{>57}$ was corrected for the contributions from each of the backgrounds described above, as well as for the effect of the false rejection of good RMC events due to the prompt cut (see Table II). In addition, $N^\gamma_{>57}$ was corrected for losses due to photon absorption in the target and due to random vetoing effects. Losses due to photon interactions in the target were estimated using the GEANT Monte Carlo simulation. Photon events were generated with the RMC energy spectrum and with initial locations sampled from reasonable stopping distri-

TABLE III. The fraction of incident muons that stopped in the target $f_{\rm stop}$, the number of dead-time corrected muon stops N_μ, the fraction of muons that undergo OMC $f_{\rm cap}$, the μ^- lifetime for each target τ_μ, and the number of photons observed with energies above 57 MeV $N^\gamma_{>57}$. The values of $f_{\rm cap}$ and τ_μ are from the results of Suzuki, Measday, and Roalsvig [30].

Target	$f_{\rm stop}$ (%)	N_μ (10^{10})	$f_{\rm cap}$ (%)	τ_μ (ns)	$N^\gamma_{>57}$
Al	91.0±2.5	4.09±0.11	60.95±0.05	864.0±1.0	1275
Si	73.5±2.0	3.85±0.11	65.86±0.05	756.0±1.0	2139
Ca	88.2±2.5	3.39±0.09	85.08±0.07	332.7±1.5	2463
Mo	81.0±4.0	3.66±0.18	95.76±0.07	99.6±1.5	1540
Sn	83.5±2.3	3.84±0.11	96.15±0.07	92.1±1.5	1286
Pb	82.3±2.2	5.51±0.15	97.10±0.05	75.4±1.0	988

TABLE IV. Contributions to the error in the branching ratios for each target, in percent.

Source of error	Al	Si	Ca	Mo	Sn	Pb
Statistics	2.8	2.7	2.0	2.5	2.8	3.2
N_μ	2.7	2.8	2.6	5.0	2.9	2.7
Photon acceptance ($\epsilon\Omega$)	4.2	4.2	4.2	4.2	4.2	4.2
Energy calibration	2.1	2.3	2.3	2.5	3.4	3.7
Photon absorption	3.0	3.0	3.0	3.0	3.0	3.0
Backgrounds	0.7	1.6	0.5	1.1	1.4	1.9
Prompt rejection	0.4	0.5	0.5	0.4	0.7	1.1
Random vetoing	0.6	0.5	0.5	0.9	0.6	0.8
$k_{\max}$	6.0	6.0	-	-	-	-
Total	9.1	9.1	6.6	8.1	7.6	8.0

butions in each of the targets. The results are listed in Table II. The error on the corrections is due to statistics in the Monte Carlo prediction and to the variation observed for various initial stopping distributions in the targets. Random vetoing refers to the loss of an otherwise acceptable event due to a veto scintillator (A, A', B) or a cosmic-ray counter firing in random coincidence, as well as the loss due to the cut requiring that no charged particle had passed through the chamber within ± 100 ns of the photon trigger. The correction was determined from the various singles rates of the counters and is listed in Table II.

The total number of incident beam particles was counted in a CAMAC scaler. The fraction of these that were muons was determined using the pulse-height and time-of-flight data from the beam counters obtained with the beam-sample trigger during each run. The fraction of these muons that stopped in the target, rather than in the surrounding scintillators, was determined by examining the pulse-heights from the scintillators. N_μ has also been corrected for pileup (two muons in the same beam bucket) and for dead time. The values for N_μ and related quantities, along with the total number of photons observed for each target are given in Table III.

The various contributions to the error in the extracted branching ratios are detailed in Table IV. The detector acceptance error is dominated by the uncertainty in the literature value for the $^{12}C(\pi^-, \gamma)$ branching ratio used in the normalization of the acceptance, but it also includes the statistical errors on the (π^-, γ) data and Monte Carlo. The error due to the uncertainty in the energy calibration was taken as the fraction of the RMC spectrum within ± 500 keV of 57 MeV. The error due to model dependence ($k_{\max}$) is explained below.

IV. RESULTS

A. Fits to the closure model polynomial

The extraction of RMC partial branching ratios from our data is slightly model dependent. RMC calculations are available for Ca [34–36], Mo, Sn, and Pb [18], but not for Al or Si. Various authors [18, 37, 38] have shown that under certain assumptions the RMC spectrum can be expressed as a polynomial of the form

$$\frac{d\Lambda_\gamma(E_\gamma)}{dE_\gamma} \propto (1 - 2x + 2x^2)x(1-x)^2, \tag{6}$$

where $x = E_\gamma / k_{\max}$. This was derived using the closure approximation, and by considering only the diagram in which the muon radiates. The use of closure assumes that all the transition strength leads to a single (average)

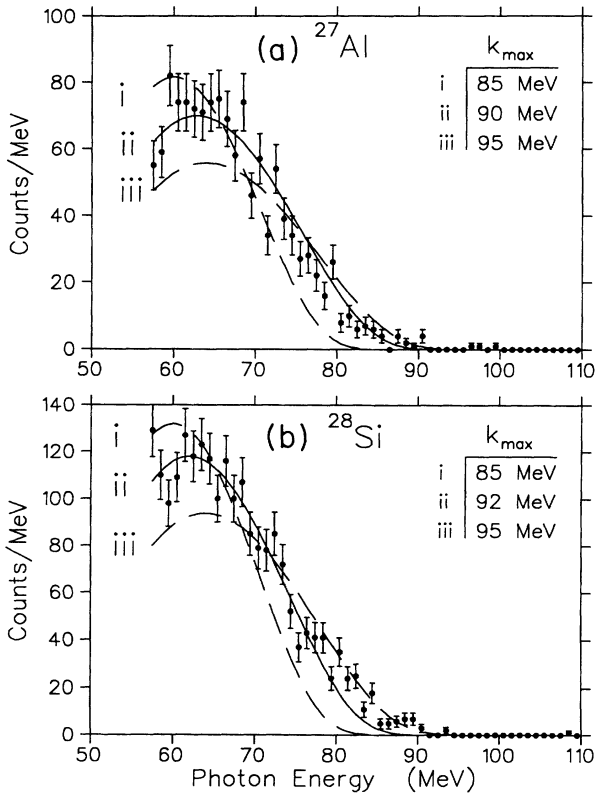

FIG. 6. Photon energy spectra from RMC on (a) Al and (b) Si, along with the spectral shapes given by Eq. (6), convoluted by the detector response function. The solid line is the spectral shape for the best-fit value of $k_{\max}$, and the dashed lines are for two other values of $k_{\max}$.

nuclear excitation energy, with a corresponding photon end-point energy $k_{\max}$. The use of the closure approximation for RMC calculations has been criticized [34], and it typically overpredicts the RMC branching ratio by large factors [39]. Nevertheless, the polynomial form given in Eq. (6) usually reproduces the spectral shape from more detailed calculations, and also fits the available data fairly well, as long as $k_{\max}$ is treated as a parameter and allowed to vary. In the absence of an RMC calculation specific to the Al and Si targets, this polynomial spectral shape was adopted to extract the branching ratios. Least-squares fits were made to the spectral shape given by Eq. (6), convoluted by the detector response, for various values of $k_{\max}$, and the value of $k_{\max}$ yielding the best fit was adopted. The error on the extracted branching ratios for Al and Si listed in Table IV due to $k_{\max}$ is due to this additional free parameter. The best-fit spectral shape is compared with the experimental spectra for Al and Si in Fig. 6. For the purposes of comparison, branching ratios were extracted for the other targets in the same way; the results are given in Table V. The results are compared with other RMC branching ratio measurements in Fig. 7.

The present results clearly confirm the reduction in RMC branching ratio with increasing atomic number for $Z > 20$, observed by Döbeli *et al.* [12]. In fact, the result for Pb is in excellent agreement with that measured by Döbeli *et al.* for the neighboring nuclide ^{209}Bi [$R_\gamma = (0.62 \pm 0.08) \times 10^{-5}$]. The branching ratio for the benchmark case of ^{40}Ca is in excellent agreement with several previous measurements [average value $(2.15 \pm 0.08) \times 10^{-5}$; see Ref. [15] and references therein]. The result for ^{27}Al is, however, in marginal disagreement with the only previous measurement [12] which gave $R_\gamma = (1.83^{+0.58}_{-0.25}) \times 10^{-5}$. It is also $\sim 3\sigma$ lower than the result for the neighboring nuclide ^{28}Si, which is measured here for the first time.

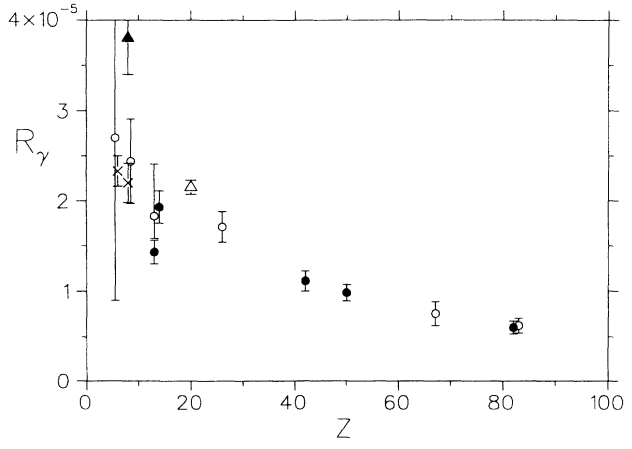

FIG. 7. RMC partial branching ratio vs the nuclear charge Z. Solid circles: this experiment; open circles: Döbeli *et al.* [12]; crosses: Armstrong *et al.* [15]; solid triangle: Frischknecht *et al.* [14]. For ^{40}Ca (open triangle) the world average of several measurements (see Ref. [15] and references therein) is shown. For the present data, the branching ratios shown are those extracted using the closure-model spectral shape (see Table V). Some data have been displaced slightly on the Z axis for clarity.

TABLE V. Partial branching ratios (R_γ) and spectrum end points ($k_{\max}$) obtained using fits to the closure-model spectral shape [Eq. (6)]. The neutron excess $\alpha = (N-Z)/A$, and the χ^2 per degree of freedom of the fit are also listed.

Target	α	R_γ (10^{-5})	$k_{\max}$ (MeV)	$\chi^2_{\rm DOF}$
Al	0.037	1.43 ± 0.13	90 ± 2	1.12
Si	0	1.93 ± 0.18	92 ± 2	1.73
Ca	0	2.09 ± 0.19	93 ± 2	1.56
Mo	0.124	1.11 ± 0.11	90 ± 2	0.82
Sn	0.157	0.98 ± 0.09	87 ± 2	1.14
Pb	0.208	0.60 ± 0.07	84 ± 3	0.85

The decrease in R_γ with increasing Z (see Fig. 7), as well as the difference between the results for ^{28}Si and ^{27}Al, are not entirely unexpected. For high-Z nuclei, the neutron Fermi momentum becomes significantly larger than that for the proton. Pauli-blocking of the final-state neutron thus reduces the available phase space, suppressing both the OMC and RMC rates. RMC is suppressed more than OMC, due to the photon in the final state, and the ratio R_γ is thus reduced. Christillin *et al.* [18], using a Fermi-gas model along with the closure approximation, and taking only the muon-radiating diagram, found that

$$R_\gamma \approx \frac{e^2}{\pi}\frac{k_{\max}^2}{m_\mu^2}(1-\alpha)\int_{57/k_{\max}}^{1}(1-2x+2x^2)x(1-x)^2dx, \tag{7}$$

where m_μ is the muon mass and $\alpha = (N-Z)/A$ is the neutron excess. While only an order of magnitude estimate, this predicts a decrease with increasing α, as well as a strong dependence on $k_{\max}$, due both to the $k_{\max}^2$ factor and to the reduction in phase space above 57 MeV in the integral as $k_{\max}$ decreases. The strong dependence of the RMC branching ratio on $k_{\max}$ in closure model calculations is well known [40]. It could account for at least part of the difference seen between Al and Si. Our data indicate a decrease in $k_{\max}$ with increasing Z for $Z > 20$, and also a lower $k_{\max}$ for Al than for Si. This, combined with the differences in α between the different targets, is in qualitative accord with the behavior of the observed partial branching ratios. Whether or not this qualitative behavior remains in a more realistic calculation of R_γ is of crucial importance, and is discussed below.

The $\sim 3\sigma$ difference between the RMC branching ratios for Al and Si may not be surprising considering the difficulty with predictions of their OMC rates. A fit to the Goulard-Primakoff [41] model for OMC rates gives the correct rate for Si [30], but underpredicts that for Al by 18%; a recent relativistic Fermi-gas model calculation [42] gets the correct rate for Al while overpredicting that for Si by 11%.

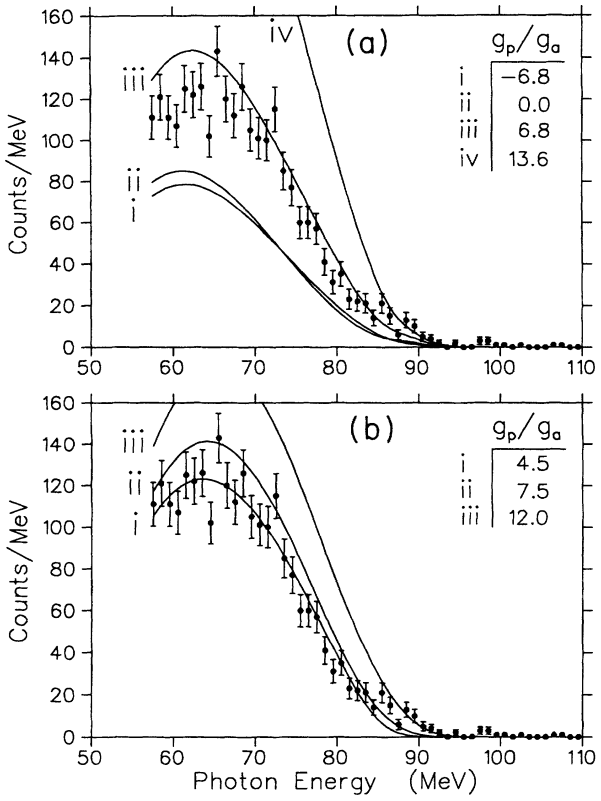

FIG. 8. Photon energy spectrum from RMC on ^{40}Ca, compared with the predictions of (a) Christillin [34] and (b) Gmitro, Ovchinnikova, and Tetereva [35] for various values of g_p. The theoretical spectra have been convoluted with the detector response function.

B. Fits to specific models

There have been many calculations of the RMC branching ratio for ^{40}Ca. Most of the early calculations [38, 43, 44] adopted the closure model and overpredict R_γ by large factors [39]. Recent theoretical work which avoids the closure approximation includes the phenomenological approach of Christillin [34], a shell-model calculation by Gmitro, Ovchinnikova, and Tetereva [35], and a sum-rule technique utilized by Roig and Navarro [36].[3] A comparison between the experimental spectrum and the predictions of Refs. [34] and [35] is given in Fig. 8. The branching ratios and values for g_p/g_a extracted from our data using each calculation are given in Table VI. The values of g_p found using the calculation of Christillin and that of Gmitro, Ovchinnikova, and Tetereva are both 1σ lower than the PCAC prediction of $g_p = 6.8 g_a$. However, the value extracted using Roig and Navarro's calculation is 1σ higher than the PCAC value. We note that the agreement between the values of g_p extracted from the phenomenological and the shell-model calculations is somewhat fortuitous, as the calculations diverge significantly in their predictions for R_γ as a function of g_p away from the PCAC value. Clearly, more theoretical work on ^{40}Ca would be welcome, especially since the experimental situation seems to be under control. Nevertheless, the results do not indicate any strong deviation from the PCAC prediction. The present results are in excellent agreement with our previous data obtained using a different apparatus, as well as several other recent measurements (see Ref. [15] for a detailed discussion of these data). A recent measurement of the photon-muon spin angular correlation in RMC on ^{40}Ca [45] also yields a value for g_p that is consistent with the PCAC value, although a lower value is favored.

The calculation of Christillin, Rosa-Clot, and Servadio [18] provided predictions for the RMC spectra as a function of g_p for a series of medium-heavy nuclei, including

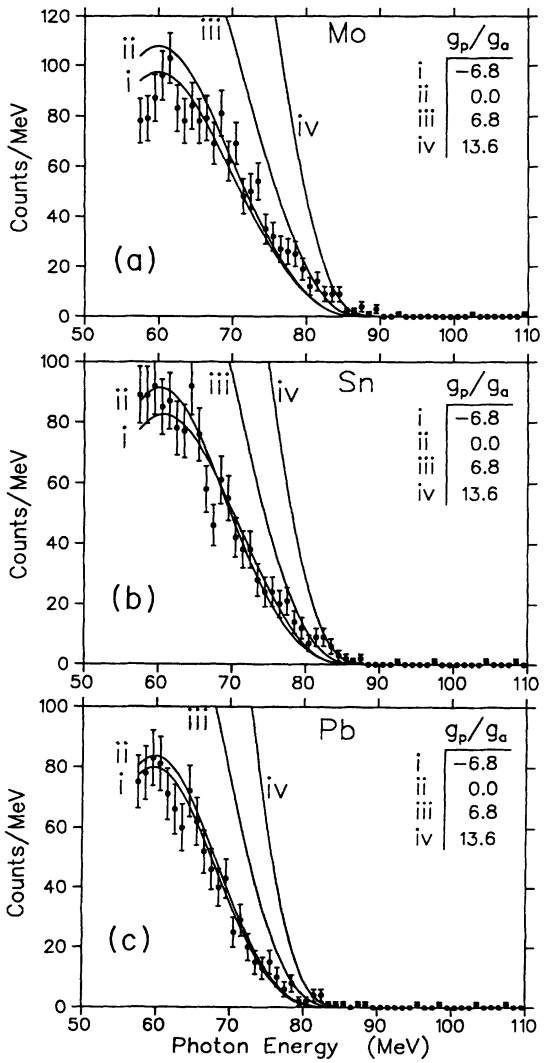

FIG. 9. Photon energy spectrum from RMC on (a) Mo, (b) Sn and (c) Pb, compared with the predictions of Christillin, Rosa-Clot, and Servadio [18] for various values of g_p. The theoretical spectra have been convoluted with the detector response function.

[3]No photon energy spectrum is available from the calculation of Roig and Navarro [36], and so the closure-model shape [Eq. (6)] was adopted to extract the branching ratio for ^{40}Ca in this case.

Mo, Sn, and Pb. Their technique avoided the closure approximation by integrating over the nuclear response obtained in a nonrelativistic Fermi-gas model. The only free parameter was an effective nucleon mass M^* to account for exchange effects, which was fixed at $M^* = 0.5M_N$ from a global fit to experimental OMC rates. The OMC results typically fit the data to a precision better than 10%. The RMC rate was then calculated in a consistent manner, neglecting recoil terms, and photon spectra were provided for different values of g_p for several nuclei. The values for the partial branching ratio and g_p extracted by comparing these spectra with our data are given in Table VI, and comparisons between the experimental spectrum and the theoretical spectra for various values of g_p are shown in Fig. 9. The small differences with the values of R_γ found using the closure model spectral shape given in Table V illustrate the slight model-dependence of the branching ratios extracted from our data. The extracted g_p for the case of Pb is given as a 1σ upper limit, since the extrapolation to large negative values of g_p for the calculation of Ref. [18] is very uncertain. The asymmetric error bars on the g_p values for Mo and Sn reflect the nonlinear dependence of R_γ on g_p in the region near $g_p = 0$.

It is tempting to interpret the present results as indicating a large "quenching" of the pseudoscalar coupling in heavy nuclei. Such a renormalization of the effective g_p when a nucleon is embedded in a nucleus has been considered by several authors and indeed a reduction in g_p in nuclear matter has been predicted [46–48]. A renormalization could arise through non-nucleonic degrees of freedom such as meson-exchange effects, the effect of the $\Delta(1232)$, modifications to the pion propagator in the nuclear medium, polarizability and screening effects, etc. However, there are several reasons to treat this conclusion with caution.

Firstly, it is clear from Fig. 9 that the experimental spectra extend to somewhat higher photon energies than predicted by the calculation; the region above $E_\gamma \sim 80$ MeV does not appear to be modeled very well. Also, the values of g_p needed to reproduce the RMC/OMC branching ratio do not agree with those needed to predict the ordinary muon capture rates in the same model; the experimental OMC rates [30] are reproduced by the calculation only for $g_p/g_a = 6.8$, the PCAC value.

More significantly, however, a recent calculation by Fearing and Welsh [49] casts some doubt on the validity of the calculation of Christillin, Rosa-Clot, and Servadio [18]. Fearing and Welsh adopt a fully relativistic Fermi-gas model along with the local-density approximation and realistic nuclear density distributions, and calculate OMC and RMC for a range of finite nuclei. This is an extension of the work of Fearing and Walker [50] wherein RMC rates for infinite nuclear matter were calculated in the same approach. The nucleon effective mass M^* is taken directly from relativistic mean field theory, rather than being treated as a free parameter, and its variation with the nuclear density is taken into account self-consistently. Other significant differences between this approach and the calculation of Ref. [18] include the use of a fully relativistic framework, the use of realistic nuclear density distributions rather than a uniform distribution and the treatment of the proton Coulomb energy and other isospin-dependent contributions to the energy difference between the initial and final states. These various refinements were found to be very important numerically, leading to changes in the predicted rates of factors of two or more.

Using the PCAC value for g_p, the resulting predictions by Fearing and Welsh [49] for the OMC rates are significantly larger than experiment, and the RMC rates are between 2–5 times as large, leading to R_γ values typically a factor of 2 larger than both our results and those of Döbeli *et al.* [12]. The discrepancy between theory and data remains even when g_p is reduced to zero or lower. Note that there were no free parameters used in the calcu-

TABLE VI. Partial branching ratios (R_γ) and values of g_p/g_a extracted from the present data using various theoretical calculations.

Target	Theory	R_γ (10^{-5})	g_p/g_a
Ca	Christillin[a]	2.21 ± 0.15	5.9 ± 0.8
	Gmitro, Ovchinnikova, and Tetereva[b]	2.07 ± 0.14	5.0 ± 1.7
	Roig and Navarro[c]	2.09 ± 0.19	7.8 ± 0.9
Mo	Christillin, Rosa-Clot, and Servadio[d]	1.26 ± 0.10	$0.0^{+1.6}_{-4.1}$
Sn	Christillin, Rosa-Clot, and Servadio[d]	1.03 ± 0.08	$0.1^{+1.4}_{-7.5}$
Pb	Christillin, Rosa-Clot, and Servadio[d]	0.60 ± 0.05	≤ 0.2

[a]Reference [34].
[b]Reference [35].
[c]Reference [36].
[d]Reference [18].

lation, aside from g_p. The predicted spectral shape tends to be enhanced at higher photon energy compared with that of Christillin *et al.*, and as already noted the data also indicate excess events in this region. The large discrepancy between the results of this calculation and the data for both OMC and RMC, along with the sensitivity of the results to the various ingredients of the calculation, leads one to question whether g_p can be reliably extracted from the data using this kind of model. Nevertheless, Fearing and Welsh [49] note that if one normalizes the predicted values of R_γ by a factor of about 0.5, the observed Z dependence for $Z \geq 20$ is matched without recourse to a Z-dependent quenching of g_p. This is in contrast to the significant renormalization of g_p required by comparing with the model of Christillin, Rosa-Clot, and Servadio [18].

Clearly, with the present theoretical situation it is not possible to make a definitive statement about the value of g_p in heavy nuclei. Calculations of the nuclear response for these nuclei using different models (e.g., a sum rule approach [36]) would be very welcome.

V. SUMMARY

The radiative muon capture partial branching ratio R_γ, for photons of energy > 57 MeV, has been measured for ^{27}Al, ^{28}Si, ^{40}Ca, $^{\text{nat}}$Mo, $^{\text{nat}}$Sn, and $^{\text{nat}}$Pb. Good agreement with previous measurements is found for the ^{40}Ca "test case." The branching ratio for ^{27}Al is 22% lower than the previous result of Döbeli *et al.* [12], and is 26% lower than that found for the neighboring nucleus ^{28}Si. The extraction of the pseudoscalar coupling constant g_p from the results for ^{27}Al and ^{28}Si awaits calculations of the nuclear response for these two nuclides. The data for the heavier nuclei confirm the Z-dependent suppression of the RMC branching ratio first observed by Döbeli *et al.* [12]. When compared with the Fermi-gas model calculation of Christillin, Rosa-Clot, and Servadio [18] these data indicate a quenching of g_p to zero for heavy nuclei. However, recent work by Fearing and Welsh [49], also based on a Fermi-gas model, but which is fully relativistic and incorporates density-dependent effects not considered in Ref. [18], does not reproduce the experimental RMC or OMC rates, and raises doubts about the ability to reliably extract g_p from the data using these types of models.

ACKNOWLEDGMENTS

We would like to thank H. Fearing and M. Welsh for providing us with results of their calculations prior to publication and for many useful discussions. T.v.E. appreciates the hospitality of TRIUMF and the RMC group. This work was supported by the National Research Council and the Natural Sciences and Engineering Research Council of Canada, the U.S. National Science Foundation, the Australian Research Council, and the Paul Scherrer Institute (Switzerland).

APPENDIX: DETECTOR RESPONSE FUNCTION

The Monte Carlo–generated spectra of the response of the detector to monoenergetic photons were fitted to a function of the form :

$$D(E_\gamma, E) = A \exp\left[-\frac{1}{2\sigma_0^2}(E - E_0)^2\right] + F \exp\left[-\frac{1}{2\sigma_3^2}(E - E_3)^2\right] \quad \text{for } E_1 < E < E_2, \quad \text{(A1)}$$

$$D(E_\gamma, E) = B \exp\left[-\frac{1}{\sigma_1}(E_1 - E)\right] + F \exp\left[-\frac{1}{2\sigma_3^2}(E - E_3)^2\right] \quad \text{for } E < E_1, \quad \text{(A2)}$$

$$D(E_\gamma, E) = C \exp\left[-\frac{1}{\sigma_2}(E - E_2)\right] + F \exp\left[-\frac{1}{2\sigma_3^2}(E - E_3)^2\right] \quad \text{for } E > E_2, \quad \text{(A3)}$$

where $E_1 = E_0 - \frac{\sigma_0^2}{\sigma_1}$, $E_2 = E_0 + \frac{\sigma_0^2}{\sigma_2}$, $B = A \exp\left[-\frac{\sigma_0^2}{2\sigma_1^2}\right]$, $C = A \exp\left[-\frac{\sigma_0^2}{2\sigma_2^2}\right]$, and A, F, E_0, E_3, σ_0, σ_1, σ_2, and σ_3 are free parameters. E_γ is the actual photon energy and E is the reconstructed energy. In the energy range of interest, this function, while somewhat arbitrary, was found to represent the Monte Carlo results quite well. The function is essentially a Gaussian with low- and high-energy tails, and with a smaller second Gaussian added (the term involving F) in order to enhance the low-energy tail of the response for high-energy photons. This second Gaussian was not required for low-energy photons, so F

TABLE VII. Coefficients of polynomial fits to the energy dependence of the photon response function parameters. The fits are for 40 MeV < E_γ < 140 MeV.

Parameter	P_0 (MeV)	P_1	P_2 $(\text{MeV})^{-1}$
σ_0	−0.5836	0.0352	
σ_1	−5.879	0.1653	-5.149×10^{-4}
σ_2	1.596	−0.03859	3.883×10^{-4}
σ_3	−47.80	1.010	-4.406×10^{-3}
E_3	1.068	0.7507	
E_0 ($E_\gamma > 60$)	−1.161	0.9481	1.724×10^{-4}
E_0 ($E_\gamma < 60$)	22.73	0.1995	5.993×10^{-3}

TABLE VIII. Coefficients of polynomial fits to the energy dependence of the photon acceptance parameters. The fits are for 40 MeV $< E_\gamma <$ 140 MeV.

Parameter	P_0	P_1 $(\text{MeV})^{-1}$	P_2 $(\text{MeV})^{-2}$	P_3 $(\text{MeV})^{-3}$
A	3.259×10^{-4}	-4.120×10^{-4}	1.015×10^{-5}	-4.050×10^{-8}
F/A	-0.1337	2.828×10^{-3}	-9.701×10^{-6}	

was set to zero for $E_\gamma < 60$ MeV. The parameters E_0, A, F/A, σ_0, σ_1, σ_2, and σ_3 were then fitted to polynomial functions of E_γ, e.g.,

$$\sigma_1 = P_0 + P_1 E_\gamma + P_2 E_\gamma^2 \ , \tag{A4}$$

over the range 40 MeV $< E_\gamma <$ 140 MeV. The coefficients of the polynomial fits are given in Tables VII and VIII.

With the detector response function parameterized in this way, the prediction for any theoretical photon spectrum was produced analytically, avoiding the need to run many lengthy Monte Carlo simulations. Also, future theoretical calculations of RMC can quite easily be convoluted with this response function and compared with our data without the need for additional Monte Carlo simulations.

[1] L. Grenacs, Annu. Rev. Nucl. Part. Sci. **35**, 455 (1985).
[2] L. Wolfenstein, in *High Energy Physics and Nuclear Structure*, edited by S. Devons (Plenum, New York, 1970), p. 661.
[3] M.L. Goldberger and S.B. Treiman, Phys. Rev. **110**, 1178 (1958).
[4] D.H. Wright *et al.*, in *Proceedings of the 4th International Conference on Intersections between Particle and Nuclear Physics,* Tucson, AZ, 1991, edited by W.T.H. Van Oers, AIP Conf. Proc. No. 243 (AIP, New York, 1992), p. 789.
[5] W. Schott *et al.*, in *Proceedings of the 1991 Lake Louise Winter Institute*, Lake Louise, Canada, 1991 (World Scientific, Singapore, in press).
[6] M. Rho, Annu. Rev. Nucl. Part. Sci. **34**, 531 (1984).
[7] B. Buck and S.M. Perez, Phys. Rev. Lett. **50**, 1975 (1983).
[8] G. Azuelos and J.E. Kitching, Nucl. Phys. **A285**, 19 (1977).
[9] D.H. Wilkinson, Nucl. Phys. **A209**, 470 (1973).
[10] G. Conforto, M. Conversi, and L. di Lella, Phys. Rev. Lett. **9**, 22 (1962).
[11] R.D. Hart, C.R. Cox, G.W. Dodson, M. Eckhause, J.R. Kane, M.S. Pandey, A.M. Rushton, R.T. Siegel, and R.E. Welsh, Phys. Rev. Lett. **39**, 399 (1977).
[12] M. Döbeli, M. Doser, L. van Elmbt, M.W. Schaad, P. Truöl, A. Bay, J.P. Perroud, J. Imazato, and T. Ishikawa, Phys. Rev. C **37**, 1633 (1988).
[13] C.J. Virtue, Ph.D. thesis, University of British Columbia (1987).
[14] A. Frischknecht *et al.*, Phys. Rev. C **32**, 1506 (1985).
[15] D.S. Armstrong *et al.*, Phys. Rev. C **43**, 1425 (1991).
[16] D.S. Armstrong *et al.*, Phys. Rev. C **40**, R1100 (1989).
[17] A. Frischknecht *et al.*, Phys. Rev. C **38**, 1996 (1988).
[18] P. Christillin, M. Rosa-Clot, and S. Servadio, Nucl. Phys. **A345**, 331 (1980).
[19] E.W. Blackmore *et al.*, Nucl. Instrum. Methods **A234**, 235 (1985).
[20] D.H. Wright *et al.*, Nucl. Instrum. Methods (in press).
[21] R.S. Henderson, R.J. Dawson, M.D. Hasinoff, G. Azuelos, S. Ahmad, A. Serna-Angel, M. Blecher, T.P. Gorringe, B.C. Robertson, and D.H. Wright, IEEE Trans. Nucl. Sci. **37**, 1116 (1990).
[22] A. Serna-Angel, Ph.D. thesis, Virginia Polytechnic Institute and State University (1991).
[23] L. Bird, R.G. Findlay, A.A. Raffler, and T. Oshka, Nucl. Instrum. Methods **166**, 155 (1979).
[24] T. Barklow, T. Glanzman, A.J. Lankford, and K. Riles, IEEE Trans. Nucl. Sci. **33**, 775 (1986).
[25] P. Bennett, M. Blecher, R. Chan, S. Daviel, M. Hasinoff, S. Ko, R. Poutissou, D. Sample, and D. Wright, IEEE Trans. Nucl. Sci. **37**, 1200 (1990).
[26] R. Brun, F. Bruyant, M. Maire, A.C. McPherson, and P. Zanarini, GEANT3 (1986); CERN Report No. DD/EE/84-1 (unpublished).
[27] J.P. Perroud *et al.*, Nucl. Phys. **A453**, 542 (1986).
[28] J.A. Bistirlich, K.M. Crowe, A.S.L. Parsons, P. Skarek, and P. Truöl, Phys. Rev. C **5**, 1867 (1972).
[29] J. Spuller, D. Berghofer, M.D. Hasinoff, R. MacDonald, D.F. Measday, M. Salomon, T. Suzuki, J-M. Poutissou, R. Poutissou, and J.K.P. Lee, Phys. Lett. **67B**, 479 (1977).
[30] T. Suzuki, D.F. Measday, and J.P. Roalsvig, Phys. Rev. C **35**, 2212 (1987).
[31] P. Hänggi, R.D. Viollier, U. Raff, and K. Alder, Phys. Lett. **51B**, 119 (1974).
[32] F. Herzog and K. Alder, Helv. Phys. Acta. **53**, 53 (1980).
[33] W. Eichenberger, R. Engfer, and A. van der Schaaf, Nucl. Phys. **A412**, 523 (1984).
[34] P. Christillin, Nucl. Phys. **A362**, 391 (1981).
[35] M. Gmitro, A.A. Ovchinnikova, and T.V. Tetereva, Nucl. Phys. **A453**, 685 (1986).
[36] F. Roig and J. Navarro, Phys. Lett. B **236**, 393 (1990).
[37] H. Primakoff, Rev. Mod. Phys. **31**, 802 (1959).
[38] H.P.C. Rood and H.A. Tolhoek, Nucl. Phys. **70**, 658 (1965).
[39] M. Gmitro and P. Truöl, Adv. Nucl. Phys. **18**, 241 (1987).
[40] R.S. Sloboda and H.W. Fearing, Phys. Rev. C **18**, 2265 (1978).
[41] B. Goulard and H. Primakoff, Phys. Rev. C **10**, 2034 (1974).
[42] H.C. Chiang, E. Oset, and P. Fernández Córdoba, Nucl.

Phys. **A510**, 591 (1990).
[43] H.W. Fearing, Phys. Rev. **146**, 723 (1966).
[44] E. Borchi and S. De Gennaro, Phys. Rev. C **2**, 1012 (1970).
[45] C.J. Virtue, K.A. Aniol, F.E. Entezami, M.D. Hasinoff, D. Horváth, H.W. Roser, and B.C. Robertson, Nucl. Phys. **A517**, 509 (1990).
[46] J. Delorme, M. Ericson, A. Figureau, and C. Thévenet, Ann. Phys. (N.Y.) **102**, 273 (1976).
[47] K. Ohta and M. Wakamatsu, Phys. Lett. **51B**, 325 (1974).
[48] E. Kh. Akhmedov, Pis'ma Zh. Eksp. Teor. Fiz. **34**, 144 (1981) [JETP Lett. **34**, 138 (1981)].
[49] H.W. Fearing and M. S. Welsh, submitted to Phys. Rev. C; TRIUMF Report No. PP-91-75 (1991).
[50] H.W. Fearing and G.E. Walker, Phys. Rev. C **39**, 2349 (1989).